


 Cite this: *RSC Adv.*, 2019, **9**, 7803

 Received 30th January 2019
 Accepted 16th February 2019

 DOI: 10.1039/c9ra00799g
 rsc.li/rsc-advances

A MnO_2 –[Ru(dpp)₃]Cl₂ system for colorimetric and fluorimetric dual-readout detection of H₂O₂

 Yuan Zhang,^a Kewei Hu,^b Zhenbao Ling^{*a} and Weihua Di^{†b}

Two-dimensional (2D) MnO_2 nanosheets were synthesized by a template-free and one-step route, and the dye [Ru(dpp)₃]Cl₂ was linked onto the MnO_2 nanosheet surface *via* electrostatic interaction. The formed MnO_2 –[Ru(dpp)₃]Cl₂ hybrid was used for a dual optical detection for H₂O₂, an important reactive oxygen species (ROS). Upon addition of H₂O₂, the reaction of MnO_2 with H₂O₂ results in the dissolution of MnO_2 nanosheets and simultaneous generation of O₂. The fading of the solution and simultaneous fluorescence change of [Ru(dpp)₃]Cl₂, sensitive to O₂, enables colorimetric and fluorimetric dual-mode detection of H₂O₂. The dual-output assay in a single probe provides a good sensitivity with a detection limit of 0.18 μM H₂O₂. The dual-signal strategy can efficiently overcome the shortcoming of the single detection mode, and improve the detection accuracy by an additional correction of output signals from each other. Moreover, the successful determination of H₂O₂ in the serum samples demonstrates the potential applicability of the MnO_2 –[Ru(dpp)₃]Cl₂ based probe in biosensing and bioanalysis.

1. Introduction

Hydrogen peroxide (H₂O₂), one of the most important reactive oxygen species (ROS), is present in various biological tissues, and plays critical roles in redox biology and cell signaling.^{1–4} Misregulation of H₂O₂ can produce and accumulate oxidative stress inside cells, resulting in damage to biomolecules such as DNA, proteins, and lipids. In the long term, this damage leads to various disorders, such as neurodegeneration, HIV activation, cardiovascular diseases, cancer and aging.^{5–10} Also, H₂O₂ is a main intermediate or final product of many enzymatic reactions by a large number of oxidases, thus enabling quantitative assays of the activity of the enzyme as well as various enzyme substrates such as protein and carbohydrate in living organisms *via* a H₂O₂-mediated process.^{11–15} Therefore, the accurate and sensitive detection of H₂O₂ is essential to evaluate its concentration in various biological events and understand the related biological effects.

To date, various analytical techniques have been developed for the detection of H₂O₂, such as high performance liquid chromatography (HPLC) detection,¹⁶ optical sensing,^{17–21} colorimetric method,^{22–25} electrochemical analysis,^{26–28} etc. It is well known that colorimetric and fluorimetric methods are relatively simple, rapid and low cost, but they are of high sensitivity and specificity, and thus they are the typical sensing techniques of optical sensors, which can be easily transformed molecular

events into fluorescence intensity or color changes. Colorimetric detection is usually achieved by monitoring the absorbance variation at a specific wavelength induced by the analyte concentration. Moreover, this method permits “naked eye” detection *via* color change with no requirement for sophisticated instrumentation.^{29,30} Fluorimetric methods are performed with the assistance of suitable probes, whose fluorescent signals respond to their interactions with analytes *via* photo-induced electron transfer (PET), fluorescence resonance energy transfer (FRET) and inner filter effect (IFE).^{30–32}

It is of great interest to integrate both optical modes into one sensor, by a fluorimetric and colorimetric dual mode strategy, which can minimize the measurement errors and has been proven to be more efficient than the single mode method.³³ Compared with the single-readout analytical strategy, the dual-readout nanomaterials-based protocols endow sensors with improved exactness and increased sensitivity. Commonly, two individual readout probes are combined to realize this dual-readout strategy, which probably complicates the detection process and even leads to unexpected interference. Therefore, a single probe with dual-readout performance was distinctly superior to the combinations of two individual probes in the dual-readout design.^{34–37}

In this work, two-dimensional (2D) MnO_2 nanosheets were synthesized by a template-free redox route, and the dye [Ru(dpp)₃]Cl₂ was linked onto the surface of MnO_2 nanosheets *via* an electrostatic interaction. The formed MnO_2 –[Ru(dpp)₃]Cl₂ hybrid was used for a colorimetric and fluorimetric detection of H₂O₂, performing the dual-output assay in a single probe. The dual-signal detection strategy in a single probe can

^aCollege of Instrumentation and Electrical Engineering, Jilin University, Changchun 130022, People's Republic of China. E-mail: lingzhenbao@jlu.edu.cn

^bState Key Laboratory on Integrated Optoelectronics, College of Electronic Science and Engineering, Jilin University, Changchun 130012, People's Republic of China. E-mail: whdi@jlu.edu.cn



hold an additional correction of output signals from each other, thus improving the detection accuracy.

2. Experimental

2.1. Chemicals

Analytical grade KMnO_4 , sodium dodecyl sulfate (SDS), concentrated sulfuric acid (H_2SO_4), hydrogen peroxide (H_2O_2) were obtained from Beijing Chemicals Reagents. $[\text{Ru}(\text{dpp})_3]\text{Cl}_2$ was purchased from Sigma-Aldrich Co. (Shanghai, China). MilliQ water was used throughout. All other chemical reagents were of analytical reagent grade. The citrate buffer was prepared by mixing an approximate ratio of citric acid and sodium citrate solutions.

2.2. Synthesis of MnO_2 nanosheets

MnO_2 nanosheets were synthesized according to previous publications.³⁸ Typically, 32 mL of SDS solution (0.1 M) and 1.6 mL of H_2SO_4 solution (0.1 M) were added into 283.2 mL distilled water and heated at 95 °C for 15 min. 3.2 mL of KMnO_4 solution (0.05 M) was added into the above solution quickly to start the reaction, and the reaction mixture was maintained at 95 °C for 60 min. In this process, the initial KMnO_4 solution with purplish red color was gradually transformed to the dark brown colloidal suspension. The resulting suspensions were centrifuged, and the precipitates were thoroughly washed with ethanol for 3 times and subsequently dried in air at 50 °C for various analyses. The purified MnO_2 was dispersed in MilliQ water to form a colloidal suspension for analyte detection.

2.3. Preparation of $\text{MnO}_2/[\text{Ru}(\text{dpp})_3]\text{Cl}_2$ hybrid

A specified concentration (20 $\mu\text{g mL}^{-1}$) of MnO_2 nanosheets and 50 μM of $[\text{Ru}(\text{dpp})_3]\text{Cl}_2$ were added to ethanol, ultrasonicated at room temperature for 30 min and left overnight. Then, they were centrifuged at 12 000 rpm for 15 min to remove the supernatant. The precipitates were dissolved in aqueous solution.

2.4. Characterizations

The X-ray powder diffraction (XRD) data were collected on an X'Pert MPD Philips diffractometer (CuK α X-radiation at 40 kV and 50 mA) with a scanning step of 0.02°. The transmission electron microscopy (TEM) observations were carried out using a JEOL 2200FS microscope. Samples for TEM investigations were prepared by first dispersing the particles in ethanol under assistance of ultrasonification and then dropping one drop of the suspension on a copper TEM grid coated with a holey carbon film. Fourier transform infrared (FT-IR) spectra (Mattson 5000) of the samples were measured in the range of 4000–450 cm^{-1} in transmission mode. The pellets were prepared by adding 0.8 mg of the sample powder to 80 mg of KBr. The powders were mixed homogeneously and compressed at a pressure of 10 KPa to form transparent pellets. X-ray photoelectron spectroscopy (XPS) analysis was performed using a PHI Quantera SXM (ULVAC-PHI) device operating at a pressure of 10^{-8} torr. The photoelectron emission spectra were recorded

using a monochromatic Al K α source (100 W). The angle between the X-ray direction and the emitted electron direction was 45°. The UV-vis absorbance measurements were carried out using a Schimadzu UV-2550 scanning spectrophotometer with a scan rate of 240 nm min^{-1} . The zeta potential measurements were conducted on the same Malvern Nano ZS instrument. The fluorescent response and emission spectrum of the sensor were measured using a 1 cm glass cuvette at 25 °C in citrate buffer (pH 5.6) with a fluorescence spectrophotometer (Hitachi F-4500, Japan) equipped with a xenon lamp. All response curves were acquired with an excitation wavelength of 535 nm. The fluorescence intensity of $\text{MnO}_2/[\text{Ru}(\text{dpp})_3]\text{Cl}_2$ (10 $\mu\text{g mL}^{-1}$) at 625 nm as a function of time was recorded by adding 30 μL of H_2O_2 solution to 3 mL of $\text{MnO}_2/[\text{Ru}(\text{dpp})_3]\text{Cl}_2$ suspensions.

2.5. H_2O_2 detection

H_2O_2 detection was conducted in an open cuvette configuration. In a typical process of H_2O_2 detection, 2 mL of $\text{MnO}_2/[\text{Ru}(\text{dpp})_3]\text{Cl}_2$ solution (10 $\mu\text{g mL}^{-1}$) was added to an open cuvette, and a given concentration of H_2O_2 solution was then added slowly. After reaction 5 min, the emission spectrum of $[\text{Ru}(\text{dpp})_3]\text{Cl}_2$ was recorded immediately with an excitation of 535 nm.

3. Results and discussion

3.1. Synthesis and characterization of MnO_2 nanosheets and $\text{MnO}_2/[\text{Ru}(\text{dpp})_3]\text{Cl}_2$ hybrid

A template-free and one-step method was used to synthesize the MnO_2 nanosheets *via* a redox reaction of KMnO_4 and sodium dodecyl sulfate (SDS). The crystal structure of the synthesized product was characterized by XRD. The XRD profile shown in Fig. 1(a) exhibited four characteristic peaks at 2 theta = 12.1°, 24.2°, 36.7°, 66°, indicating a typical lamellar structure. All the diffraction peaks can be well indexed to $\delta\text{-MnO}_2$ phase (JCPDS no. 18-0802). Fig. 1(b) shows a TEM image of representative areas of the as-synthesized product. The sample was typically composed of ultrathin and transparent lamellar structure with ample graphene-like wrinkles and folds, displaying a typical 2D morphology of MnO_2 nanosheets.³⁹ The perceived average lateral dimension of the nanosheets is estimated to be ~200 nm.

The FT-IR spectrum (Fig. 1(c)) provides further insight into the structure and surface state of synthesized MnO_2 . The peaks at 518, 473 cm^{-1} are assigned to the characteristic absorption of the Mn–O stretching vibration of octahedral $[\text{MnO}_6]$ framework.^{40,41} Two intense bands at 3420 and 1625 cm^{-1} are attributed to the physically adsorbed water and the interlayer water in the MnO_2 nanosheets.⁴⁰ The low intensity of peaks in the 2922–2995 cm^{-1} region are assignable to the asymmetric and symmetric $-\text{CH}_2$ and $-\text{CH}_3$ stretching due to the use of SDS in the synthesis.⁴²

XPS was used to make a qualitative analysis of chemical valence and binding of the element for the synthesized MnO_2 . Two characteristic peaks centered at 642.2 and 654.1 eV correspond to Mn 2p_{3/2} and Mn 2p_{1/2} of MnO_2 , respectively (Fig. 1(d)).^{40,43} The spin-energy separation of ~11.9 eV is also



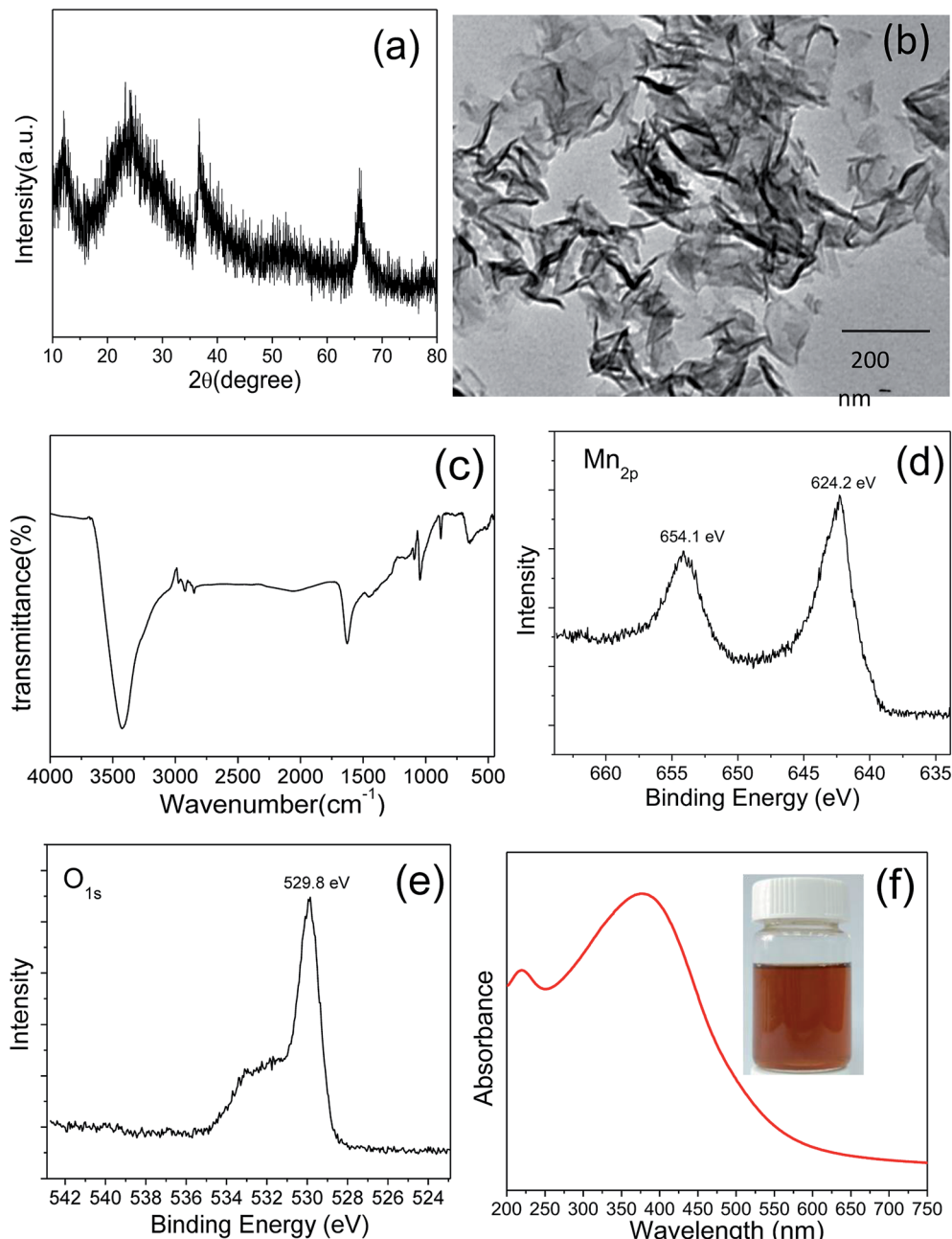


Fig. 1 XRD pattern (a), TEM image (b), FT-IR spectrum (c), XPS spectra of $\text{Mn}_{2\text{p}}$ (d) and $\text{O}_{1\text{s}}$ (e), and UV-vis absorption spectrum (f) of the synthesized MnO_2 nanosheets.

consistent with those previous reports by other research groups.^{40,44} No additional signals attributed to Mn_2O_3 and KMnO_4 were found in the XPS spectrum, indicating the generation of pure MnO_2 . The XPS spectrum of oxygen exhibits two peaks centered at 529.8 and 532.7 eV (Fig. 1(e)), which are assigned to the lattice oxygen of $[\text{MnO}_6]$ octahedra and the oxygen in the interlayer H_2O or H_3O^+ , in good agreement with the FTIR result.⁴⁰

The UV-vis absorption spectrum (Fig. 1(f)) of the synthesized MnO_2 solution exhibits a broad absorption band around ~ 375 nm, which is attributed to the d-d transition of $\text{Mn}(\text{IV})$ in

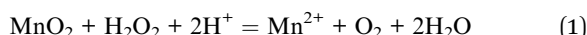
the octahedral $[\text{MnO}_6]$ unit. The wavelength and intensity of the absorbance are in line with the previous findings of single-layer MnO_2 nanosheets by other groups.^{45–47} The colloidal suspension of single-layer MnO_2 nanosheets shows good stability and remains stable at 4°C in the dark for more than 15 days without any precipitates.

The dye $[\text{Ru}(\text{dpp})_3]\text{Cl}_2$ was linked onto the MnO_2 nanosheet surface *via* an electrostatic interaction. In order to verify the interaction between MnO_2 nanosheets and $[\text{Ru}(\text{dpp})_3]\text{Cl}_2$, the zeta potential of MnO_2 nanosheets was measured. The zeta potential of MnO_2 nanosheets was 57.2 mV (pH = 7), while it

decreased to 36.5 mV as MnO_2 nanosheets were treated with $[\text{Ru}(\text{dpp})_3]\text{Cl}_2$. This indicates that there exists an electrostatic interaction, leading to the conjugation of $[\text{Ru}(\text{dpp})_3]\text{Cl}_2$ at the surface of MnO_2 nanosheets. This indicates that $[\text{Ru}(\text{dpp})_3]\text{Cl}_2$ could be linked onto the MnO_2 nanosheets *via* an electrostatic interaction.

3.2. Design of dual-signal assay for H_2O_2 in a single probe

The present sensor for H_2O_2 detection consists of MnO_2 nanosheets and an oxygen responsive fluorescent transducer, $[\text{Ru}(\text{dpp})_3]\text{Cl}_2$. The as-synthesized MnO_2 nanosheets were firstly incubated with the dye $[\text{Ru}(\text{dpp})_3]\text{Cl}_2$, and the dye $[\text{Ru}(\text{dpp})_3]\text{Cl}_2$ was linked onto the surface of MnO_2 nanosheets by an electrostatic interaction. Upon the addition of H_2O_2 , MnO_2 nanosheets interact with H_2O_2 *via* a redox reaction following the eqn (1), resulting in the dissolution of MnO_2 nanosheets, which makes the solution fade gradually, enabling the colorimetric detection of H_2O_2 . Meanwhile, the *in situ* generated O_2 in the reaction of MnO_2 with H_2O_2 quenches the luminescence of $[\text{Ru}(\text{dpp})_3]\text{Cl}_2$ that is an O_2 -sensitive phosphorescent dye.⁴⁸ The changes of oxygen concentration induced by H_2O_2 addition can be transformed into a fluorescence signal using an oxygen responsive transducer, enabling the fluorimetric detection of H_2O_2 . Therefore, the present MnO_2 - $[\text{Ru}(\text{dpp})_3]\text{Cl}_2$ system enables a dual optical detection of H_2O_2 , performing the dual readout assay in a single probe.



3.3. Optimization of the sensing system

To verify whether the above dual readout sensing principle for H_2O_2 detection is feasible, we conducted a preliminary experiment that a small amount of H_2O_2 was tentatively added to the MnO_2 - $[\text{Ru}(\text{dpp})_3]\text{Cl}_2$ system. The fading of MnO_2 solution was observed; meanwhile, the luminescence of $[\text{Ru}(\text{dpp})_3]\text{Cl}_2$ was decreased, indicating the feasibility of sensing strategy.

The sensing performances can be influenced by several factors, such as reaction pH value, incubation time of MnO_2 and $[\text{Ru}(\text{dpp})_3]\text{Cl}_2$ and so on. Therefore, these experimental parameters should be systematically optimized for H_2O_2 detection. The effect of the incubation time of MnO_2 and $[\text{Ru}(\text{dpp})_3]\text{Cl}_2$ on H_2O_2 detection was investigated. In the preparation process, the MnO_2 nanosheets were first incubated with the dye $[\text{Ru}(\text{dpp})_3]\text{Cl}_2$, and then centrifuged. The incubation time has significant influence on the numbers of $[\text{Ru}(\text{dpp})_3]\text{Cl}_2$ molecule linked onto the surface of MnO_2 nanosheets. With the increase of incubation time, the luminescence of $[\text{Ru}(\text{dpp})_3]\text{Cl}_2$ increases. Up to 30 min, the luminescence was no longer increased. Thus, the incubation time of 30 min was chosen for the preparation of MnO_2 - $[\text{Ru}(\text{dpp})_3]\text{Cl}_2$ sample.

The reactivity of MnO_2 with H_2O_2 was found to be strongly dependent on the solution pH value. To demonstrate the effect of solution pH on the reactivity of MnO_2 with H_2O_2 , the experiments were conducted as below. The equivalent quantities of

MnO_2 were dispersed in 5 mL citrate buffer with different pH values ranging from 4.8 to 6.5 and MilliQ water with pH 7.4, respectively. Then, 50 μL of H_2O_2 solution (100 μM) was immediately added and reacted at room temperature for 3 min. The supernatant was immediately moved to a quartz cuvette for UV-vis absorption measurement. The absorbance of MnO_2 solution with the addition of H_2O_2 decreases remarkably with the decrease of pH value (Fig. 2). For a parallel comparison, we also measured the absorption spectra of MnO_2 solution under different pH conditions, but without the addition of H_2O_2 . We can see that the absorbance of MnO_2 solution without the addition of H_2O_2 decreases slightly with the decrease of pH values ranging from 7.4 to 4.8, indicating a slight decomposition of MnO_2 nanosheets under an acidic condition. In contrast, the absorbance of MnO_2 solution with the addition of H_2O_2 decreases remarkably (Fig. 2). The above results indicate that an acidic reaction condition benefits the reaction of MnO_2 nanosheets with H_2O_2 , and that the presence of H_2O_2 remarkably accelerates the decomposition of MnO_2 in acidic solution. It is also considered that the speed of O_2 release cannot be too fast during H_2O_2 detection. Here, the citrate buffer of pH 5.6 was chosen for H_2O_2 detection.

3.4. Colorimetric detection of H_2O_2

Fig. 3 shows the UV-vis absorption spectra of MnO_2 solution after reaction upon the addition of various concentrations of H_2O_2 at pH 5.6. All UV-vis absorption spectra exhibited a broad band around 375 nm that originates from the d-d transition of Mn(IV) in the octahedral $[\text{MnO}_6]$ unit.³⁸ With an increase of H_2O_2 concentration, the absorbance of the solution decreases gradually due to the reduction of MnO_2 to Mn^{2+} by H_2O_2 . Indeed, the variation of color depth of the solution as a result of the change of H_2O_2 concentration added can be observed directly by the naked eyes, as shown in the photographs taken for samples treated with various concentrations of H_2O_2 (inset of Fig. (2)). With the increase of H_2O_2 concentration added, the solution

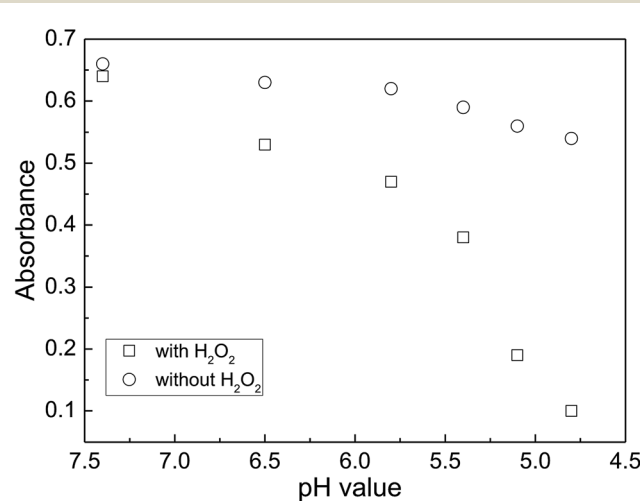


Fig. 2 A comparison of the MnO_2 solution absorbance with and without the addition of H_2O_2 under the reaction conditions with different pH values. The reaction time was fixed at 3 min.



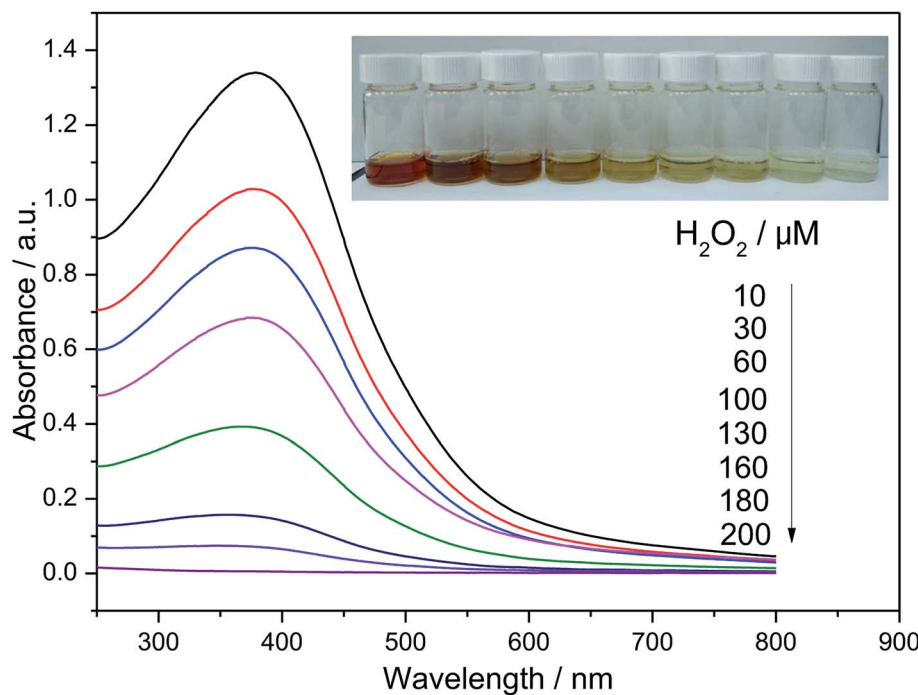


Fig. 3 UV-vis absorption spectra of MnO_2 solution upon the addition of H_2O_2 solution with various concentrations. The inset shows the corresponding photographs of the reaction solution.

faded gradually. The absorbance exhibits a good linear relationship against H_2O_2 concentration in the range of 0–200 μM . By a linear fitting, the regression equation for H_2O_2 was $A = 1.464 - 7370[\text{H}_2\text{O}_2]$ (M), where A represents the absorbance of the resulting solution at a given H_2O_2 concentration added. Thus, this colorimetric method provides a simple, low-cost and convenient assay for H_2O_2 since the synthesis of MnO_2 nanosheets is quite simple and this method does not need expensive instruments and complicated operations.

3.5. Fluorimetric detection of H_2O_2

3.5.1. Fluorescence response toward H_2O_2 . When H_2O_2 was added to the MnO_2 – $[\text{Ru}(\text{dpp})_3]\text{Cl}_2$ system, the luminescence of $[\text{Ru}(\text{dpp})_3]\text{Cl}_2$ sensitive to O_2 was gradually quenched under 535 nm excitation due to the generation of O_2 . To know the overall luminescence response process with time after the addition of H_2O_2 to MnO_2 – $[\text{Ru}(\text{dpp})_3]\text{Cl}_2$, the emission of $[\text{Ru}(\text{dpp})_3]\text{Cl}_2$ at 625 nm was monitored continuously in a cuvette by a general fluorometer as a function of time. Fig. 4 shows the time-scanning curves of the emission intensities of $[\text{Ru}(\text{dpp})_3]\text{Cl}_2$ at 625 nm upon addition of various concentrations of H_2O_2 . It is clearly seen that the luminescence change of $[\text{Ru}(\text{dpp})_3]\text{Cl}_2$ depends on time after adding H_2O_2 . Overall, the emission intensity of $[\text{Ru}(\text{dpp})_3]\text{Cl}_2$ decreased gradually upon time when a certain concentration of H_2O_2 was added to MnO_2 – $[\text{Ru}(\text{dpp})_3]\text{Cl}_2$ system. The luminescence change is fast at first, and then slows down. Also, the luminescence response is dependent on H_2O_2 concentration. We can see that the increase of H_2O_2 concentration accelerates the response of sensor. Indeed, it is not difficult to understand for time and H_2O_2

concentration dependent fluorescence change. As we know, the luminescence decrease of $[\text{Ru}(\text{dpp})_3]\text{Cl}_2$ originates from its luminescence quenching by O_2 produced *via* the reaction of MnO_2 with H_2O_2 . When a certain concentration of H_2O_2 was added, H_2O_2 molecules immediately diffused toward the MnO_2 nanosheet surfaces. At starting, the diffusion of H_2O_2 is fast due to a large driving force as a result of a large concentration gradient, so that more H_2O_2 molecules can reach and interact with the MnO_2 nanosheet surfaces, which generates more O_2 to quench the fluorescence of $[\text{Ru}(\text{dpp})_3]\text{Cl}_2$, leading to a higher degree of luminescence change. Upon the depletion of H_2O_2 , the

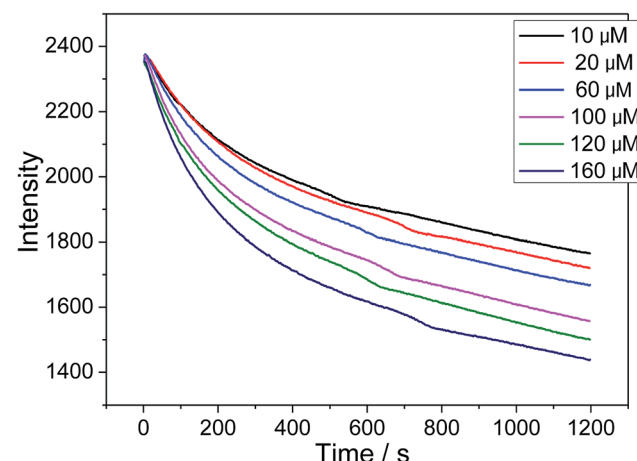


Fig. 4 Time and H_2O_2 concentration dependent luminescence response of $[\text{Ru}(\text{dpp})_3]\text{Cl}_2$ under 535 nm excitation.



luminescence change slows down with time. Similarly, we can also explain H_2O_2 concentration dependent fluorescence response, in that the addition of a higher concentration of H_2O_2 results in a quicker fluorescence response (Fig. 4).

3.5.2. Stern–Volmer plots. On the basis of the response curves acquired from Fig. 4, the emission spectra of $\text{MnO}_2\text{–}[\text{Ru}(\text{dpp})_3]\text{Cl}_2$ system treated with various concentrations of H_2O_2 were recorded at the time point when the luminescence almost reaches an equilibrium after H_2O_2 addition, as shown in Fig. 5(a). We can see that the emission intensities of $[\text{Ru}(\text{dpp})_3]\text{Cl}_2$ at 625 nm decrease gradually upon successive addition of H_2O_2 . For a clear comparison, the emission intensity of $[\text{Ru}(\text{dpp})_3]\text{Cl}_2$ at 625 nm for $\text{MnO}_2\text{–}[\text{Ru}(\text{dpp})_3]\text{Cl}_2$ treated with various concentrations of H_2O_2 were collected in Fig. 5(b). Clearly, the emission intensity drops rapidly with H_2O_2 concentration over the range of 0–200 μM , indicating a quick quenching.

The quenching of luminescence in dilute solutions is described by the Stern–Volmer relationship, as shown in the eqn (2).^{49–51}

$$F_0/F = 1 + K_{\text{SV}}[Q] \quad (2)$$

where F_0 is the initial luminescence of $\text{MnO}_2\text{–}[\text{Ru}(\text{dpp})_3]\text{Cl}_2$ system prior to H_2O_2 addition, F is the luminescence of the solution with addition of any given concentration Q of analyte and K_{SV} is the Stern–Volmer quenching constant. Providing the plot of F_0/F versus Q is linear, K_{SV} can be determined. Fig. 5(c) shows the Stern–Volmer plot of F_0/F against H_2O_2 concentration. We can see that F_0/F exhibits a good linear relationship against H_2O_2 concentration in the range of 0–200 μM with a correlation coefficient $R^2 = 0.999$, indicating a wide linear response for H_2O_2 sensing. From the Stern–Volmer plot, K_{SV} was calculated to be 22 520 M^{-1} based on eqn (2) and the linear regression equation for H_2O_2 was $F_0/F = 0.99845 + 22 520[\text{H}_2\text{O}_2]$ (M). The detection limit (LOD) was defined by the equation $\text{LOD} = (3\sigma/s)$ at the signal-to-noise of 3, where σ is the standard deviation of the blank signals ($n = 11$) and s is the slope of the calibration curve. Based on this equation, the LOD for H_2O_2 was calculated to be 0.18 μM . The relative standard deviation (RSD) was 4.7% and 3.8% for the determination of 8 μM and 68 μM of H_2O_2 ($n = 6$), respectively. The above results indicate high reproducibility and reliability of this method for H_2O_2 sensing.

3.5.3. Sensing selectivity. The selectivity of the sensor is essential for detecting an analyte accurately. To demonstrate the sensing selectivity of $\text{MnO}_2\text{–}[\text{Ru}(\text{dpp})_3]\text{Cl}_2$ toward H_2O_2 , several bio-active molecules with reducing ability, such as glucose, fructose, glutathione (GSH), and uric acid were used to check whether their presence interfere with the H_2O_2 determination (Fig. 6). Although these molecules with reducing ability reacts with MnO_2 via a redox reaction, no O_2 can release. Therefore, their existence cannot result in the luminescence quenching of $[\text{Ru}(\text{dpp})_3]\text{Cl}_2$, indicating high selectivity of our designed sensor toward H_2O_2 detection.

In addition, several common metal ions in biological fluids, such as Na^+ , K^+ , Mg^{2+} , Ca^{2+} , Cu^+ and Fe^{2+} were added to examine their influence on sensing properties (Fig. 6). The luminescence

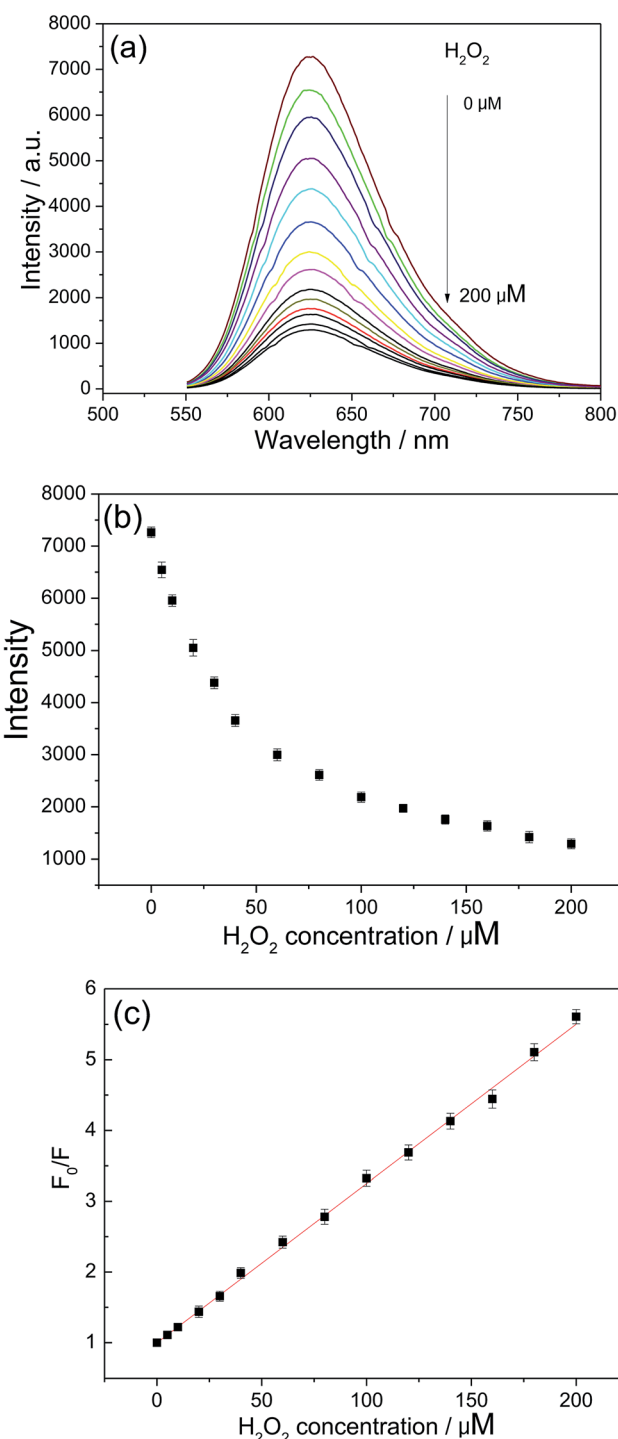


Fig. 5 (a) The emission spectra of $\text{MnO}_2\text{–}[\text{Ru}(\text{dpp})_3]\text{Cl}_2$ colloidal solution treated with various concentrations of H_2O_2 with 535 nm excitation. (b) The emission intensities of $[\text{Ru}(\text{dpp})_3]\text{Cl}_2$ at 625 nm as a function of H_2O_2 concentration. (c) Stern–Volmer plot of H_2O_2 sensing over the range of 0–200 μM H_2O_2 . The error bars represent the standard deviation.

of $[\text{Ru}(\text{dpp})_3]\text{Cl}_2$ was almost unaffected by the extra addition of a certain amount of Na^+ , K^+ , Mg^{2+} and Ca^{2+} . Even if several biologically relevant redox active metal ions, such as Cu^+ and Fe^{2+} , were introduced into this sensing system, the

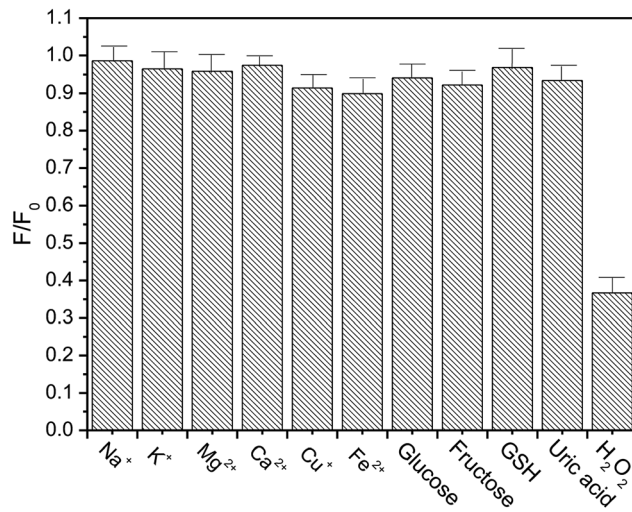


Fig. 6 The luminescence of $\text{MnO}_2\text{--}[\text{Ru}(\text{dpp})_3]\text{Cl}_2$ solution (50 μM) upon the addition of various antioxidants and bio-active metal ions. Na^+ , K^+ , Mg^{2+} and Ca^{2+} , 100 μM ; Cu^+ , Fe^{2+} , 50 μM ; glucose, fructose and uric acid, 100 μM ; H_2O_2 and GSH, 50 μM . In the vertical coordinate, F/F_0 refers to a ratio, where F_0 is the initial luminescence of $\text{MnO}_2\text{--}[\text{Ru}(\text{dpp})_3]\text{Cl}_2$ prior to any addition, F is the luminescence of the solution with addition of any given concentration of interfering substance.

Table 1 Determination of H_2O_2 in serum samples

Sample numbers	Added (μM)	Obtained by our sensor (μM)	Recovery (%)
1	20	22.5	112.5
2	50	48.1	96.2
3	100	92.5	92.5

luminescence shows only a slight change, compared with the case of added H_2O_2 . The above results indicate that the response of our present sensor toward H_2O_2 is highly selective.

3.5.4. Detection of H_2O_2 in biological samples. To demonstrate the practical application of our present sensor, the determination of H_2O_2 in the serum samples was also performed. Three concentrations of H_2O_2 were added into the serum samples. After incubation with $\text{MnO}_2\text{--}[\text{Ru}(\text{dpp})_3]\text{Cl}_2$, the fluorescence signals were detected and analyzed. The H_2O_2 concentrations in the serum samples were obtained according to the linear regression equation, and the resulting results were also listed in Table 1. The recoveries of the H_2O_2 concentration ranged from 92.5% to 112.5%, thus demonstrating the potential applicability of $\text{MnO}_2\text{--}[\text{Ru}(\text{dpp})_3]\text{Cl}_2$ based probe for the quantitative detection of H_2O_2 in biological fluids.

4. Conclusions

2D MnO_2 nanosheets were synthesized by a template-free redox route, and the dye $[\text{Ru}(\text{dpp})_3]\text{Cl}_2$ was linked onto the MnO_2 nanosheet surface *via* an electrostatic interaction. The formed $\text{MnO}_2\text{--}[\text{Ru}(\text{dpp})_3]\text{Cl}_2$ hybrid was used for a dual optical

detection of H_2O_2 . Upon addition of H_2O_2 , the fading of MnO_2 solution enables the colorimetric detection for H_2O_2 owing to the decomposition of MnO_2 . Simultaneously, the produced O_2 quenches the luminescence of $[\text{Ru}(\text{dpp})_3]\text{Cl}_2$, enabling the fluorescent detection of H_2O_2 . This sensing system responds linearly and quickly in a wide H_2O_2 concentration range of 0–200 μM , and achieves a detection limit of 0.18 μM and a relative standard deviation lower than 4.7%. The devised dual-readout sensor here could thereby be a reliable option to quantitatively detect H_2O_2 in biological and environmental samples due to additional signal correction from each other, which validated its efficiency in on-site application.

Conflicts of interest

There are no conflicts to declare.

Acknowledgements

We acknowledge financial support from the National Science Foundation of China (Grant No. 61178073, 61222508).

References

- 1 S. G. Rhee, *Science*, 2006, **312**, 1882–1883.
- 2 C. C. Winterbourn, *Nat. Chem. Biol.*, 2008, **4**, 278–286.
- 3 M. Schieber and N. S. Chandel, *Curr. Biol.*, 2014, **24**, R453–R462.
- 4 C. X. Li, S. Q. Wang, Y. M. Huang, Q. Wen, L. Wang and Y. H. Kan, *Dalton Trans.*, 2014, **43**, 5595–5602.
- 5 A. R. Lippert, G. C. V. De Bittner and C. J. Chang, *Acc. Chem. Res.*, 2011, **44**, 793–804.
- 6 K. Sinha, J. Das, P. B. Pal and P. C. Sil, *Arch. Toxicol.*, 2013, **87**, 1157–1180.
- 7 J. Xu, J. Zhai, Y. Xu, J. Zhu, Y. Qin and D. Jiang, *Analyst*, 2016, **141**, 2380–2383.
- 8 L. Zhang, M. Chen, Y. Jiang, M. Chen, Y. Ding and Q. Liu, *Sens. Actuators, B*, 2017, **239**, 28–35.
- 9 Y. Sun, M. Luo, X. Meng, J. Xiang, L. Wang, Q. Ren and S. Guo, *Anal. Chem.*, 2017, **89**, 3761–3767.
- 10 S. Ghosh, P. Roy, N. Karmodak, E. D. Jemmis and G. Mugesh, *Angew. Chem., Int. Ed.*, 2018, **57**, 4510–4515.
- 11 L. Shang, S. J. Dong and G. U. Nienhaus, *Nano Today*, 2011, **6**, 401.
- 12 G. W. Yan, Y. Zhang and W. H. Di, *Analyst*, 2018, **143**, 2915–2922.
- 13 H. Deng, G. Wu, D. He, H. Peng, A. Liu, X. Xia and W. Chen, *Analyst*, 2015, **140**, 7650–7656.
- 14 X. Peng, G. Wan, L. Wu, M. Zeng, S. Lin and G. Wang, *Sens. Actuators, B*, 2018, **257**, 166–177.
- 15 X. Zhang, X. Q. Bi, W. H. Di and W. P. Qin, *Sens. Actuators, B*, 2016, **231**, 714–722.
- 16 S. Wiesufer, A. Boddenberg, A. P. Ligon, G. Dallmann, W. V. Turner and S. Gab, *Environ. Sci. Pollut. Res.*, 2002, **4**, 41–47.
- 17 C. Tagad, S. Dugasani, R. Aiyer, S. Park, A. Kulkani and S. Sabharwal, *Sens. Actuators, B*, 2013, **183**, 144–149.



18 C. J. Lv, W. H. Di, Z. H. Liu, K. Z. Zheng and W. P. Qin, *Analyst*, 2014, **139**, 4547–4555.

19 X. Y. Shan, L. J. Chai, J. J. Ma, Z. S. Qian, J. R. Chen and H. Feng, *Analyst*, 2014, **139**, 2322–2325.

20 H. Tan, C. Ma, Q. Li, L. Wang, F. Xu, S. Chen and Y. Song, *Analyst*, 2014, **139**, 5516–5522.

21 D. Sodzel, V. Khranovskyy, V. Beni, A. P. F. Turner, R. Viter, M. O. Eriksson, P. Holtz, J. Janot, M. Bechelany, S. Balme, V. Smyntyna, E. Kolesneva, L. Dubovakaya, I. Volotovski, A. Ubelis and R. Yakimova, *Microchim. Acta*, 2015, **182**, 1819–1826.

22 H. Wei and E. Wang, *Anal. Chem.*, 2008, **80**, 2250–2254.

23 X. Chen, B. Su, Z. Cai, X. Chen and M. Oyama, *Sens. Actuators, B*, 2014, **201**, 286–292.

24 Z. C. Xing, J. Q. Tian, A. M. Asiri, A. H. Qusti, A. O. Al-Youbi and X. P. Sun, *Biosens. Bioelectron.*, 2014, **52**, 452–457.

25 Y. W. Zhang, J. Q. Tian, S. Liu, L. Wang, X. Y. Qin, W. B. Lu, G. H. Chang, Y. L. Luo, A. M. Asiri, A. O. Al-Youbi and X. P. Sun, *Analyst*, 2012, **137**, 1325–1328.

26 S. Azizi, S. Ghasemi, A. Samadi-Maybodi and M. Ranjbar, *Sens. Actuators, B*, 2015, **216**, 271–278.

27 M. Mahmoudian, Y. Alias, W. Basirun, P. Woi and M. Sookhakian, *Sens. Actuators, B*, 2014, **201**, 526–534.

28 W. Xiang, G. W. Wang, S. Cao, Q. G. Wang, X. Y. Xiao, T. Li and M. H. Yang, *Microchim. Acta*, 2018, **185**, 335.

29 L. Xu, S. Wei, Q. Diao, P. Ma, X. Liu, Y. Sun, D. Song and X. Wang, *Sens. Actuators, B*, 2017, **246**, 395–401.

30 C. Li, J. R. Zhao, Y. Q. Chen, X. Y. Wang, X. B. Sun, W. Pan, G. F. Yu, Z. Yan and J. P. Wang, *Analyst*, 2018.

31 C. Li, W. Liu, X. Sun, W. Pan and J. Wang, *Sens. Actuators, B*, 2017, **252**, 544–553.

32 J. P. Sheng, X. X. Jiang, L. Q. Wang, M. H. Yang and Y. N. Liu, *Anal. Chem.*, 2018, **90**, 2926–2932.

33 Y. Li, S. He, Y. Lu and X. Zeng, *Org. Biomol. Chem.*, 2011, **9**, 2606–2609.

34 H. Ouyang, X. Tu, Z. Fu, W. Wang, S. Fu, C. Du and Y. Lin, *Biosens. Bioelectron.*, 2018, **106**, 43–49.

35 D. Zhao, C. Chen, J. Sun and X. Yang, *Analyst*, 2016, **141**, 3280–3288.

36 C. Chen, D. Zhao, J. Sun and X. Yang, *Analyst*, 2016, **141**, 2581–2587.

37 W. S. Zou, C. H. Ye, Y. Q. Wang, W. H. Li and X. H. Huang, *Sens. Actuators, B*, 2018, **271**, 54–63.

38 W. H. Di, X. Zhang and W. P. Qin, *Appl. Surf. Sci.*, 2017, **400**, 200–205.

39 Z. N. Liu, K. L. Xu, H. Sun and S. Y. Yin, *Small*, 2015, **11**, 2182–2191.

40 G. Zhao, J. Li, L. Jiang, H. Dong, X. Wang and W. Hu, *Chem. Sci.*, 2012, **3**, 433–437.

41 S. Shi, C. J. Xu, C. Yang, Y. Y. Chen, J. J. Liu and F. Y. Kang, *Sci. Rep.*, 2013, **3**, 2598.

42 L. Z. Wang, Y. Omomo, N. Sakai, K. Fukuda, I. Nakai, Y. Ebina, K. Takada, M. Watanabe and T. Sasaki, *Chem. Mater.*, 2003, **15**, 2873–2878.

43 L. Peng, X. Peng, B. Liu, C. Wu, Y. Xie and G. Yu, *Nano Lett.*, 2013, **13**, 2151–2157.

44 L. Wei, C. Li, H. Chu and Y. Li, *Dalton Trans.*, 2011, **40**, 2332–2337.

45 Y. Omomo, T. Sasaki, L. Wang and M. Watanabe, *J. Am. Chem. Soc.*, 2003, **125**, 3568–3575.

46 L. Z. Wang, Y. Omomo, N. Sakai, K. Fukuda, I. Nakai, Y. Ebina, K. Takada, M. Watanabe and T. Sasaki, *Chem. Mater.*, 2003, **15**, 2873–2878.

47 K. Kai, Y. Yoshida, H. Kageyama, G. Saito, T. Ishigaki, Y. Furukawa and J. Kawamata, *J. Am. Chem. Soc.*, 2008, **130**, 15938–15943.

48 H. C. Chen, J. W. Tian, W. J. He and Z. J. Guo, *J. Am. Chem. Soc.*, 2015, **137**, 1539–1547.

49 D. J. Desilets, P. T. Kissinger and F. E. Lytle, *Anal. Chem.*, 1987, **59**, 1830–1834.

50 M. Shamsipur, M. Shanehasz, K. Khajeh, N. Mollania and S. H. Kazemi, *Analyst*, 2012, **137**, 5553–5559.

51 J. B. Xiao, Y. R. Zhao, F. F. Mao, J. Liu, M. X. Wu and X. B. Yu, *Analyst*, 2012, **137**, 195–201.